







THE IMPACT OF SOURCE AND SURVEY MODELLING ON THE CONNECTION BETWEEN [O III] EMITTERS AND Ly α FOREST TRANSMISSION AT $z \sim 6$

LUKE CONABOY^{1,*} , JAMES S. BOLTON¹ , LAURA C. KEATING² , MARTIN G. HAEBNELT³ , GIRISH KULKARNI⁴ ,
EWALD PUCHWEIN⁵ 

¹School of Physics and Astronomy, The University of Nottingham, University Park, Nottingham, NG7 2RD, UK

²Institute for Astronomy, University of Edinburgh, Blackford Hill, Edinburgh, EH9 3HJ, UK

³Kavli Institute for Cosmology and Institute of Astronomy, Madingley Road, Cambridge, CB3 0HA, UK

⁴Tata Institute of Fundamental Research, Homi Bhabha Road, Mumbai 400005, India and

⁵Leibniz-Institut für Astrophysik Potsdam, An der Sternwarte 16, 14482 Potsdam, Germany

Version June 3, 2026

ABSTRACT

James Webb Space Telescope (JWST) surveys of [O III]-emitting galaxies are offering fresh insight into the connection between galaxies and the intergalactic medium at redshift $z \sim 6$. Recent measurements of the cross-correlation between [O III]-emitting galaxies and Ly α forest transmission present an apparent challenge to numerical models. Here we improve upon previous theoretical work by constructing an empirical model that connects haloes with the observed population of [O III] emitters and incorporates the geometry and depth of the *JWST* surveys into mock galaxy survey catalogues. We compare these mocks to recent measurements of [O III] emitter clustering and the one and two dimensional galaxy–Ly α transmission cross-correlation. The large scatter in our mock survey measurements of the cross-correlation enables a statistically good match to the observational data, albeit the peak of the one dimensional correlation in our mocks occurs at a scale ≈ 10 cMpc below that observed. The large scatter implies that, at present, current galaxy-IGM observations may struggle to rule out a broad range of ionising source models. We anticipate that further progress will strongly benefit from increased observational sample sizes, as well as simulations performed in box sizes > 250 cMpc that use a variety of source models.

Subject headings: methods: numerical – intergalactic medium – galaxies: high-redshift – quasars: absorption lines – large scale structure of Universe – dark ages, reionization, first stars

1. INTRODUCTION

In the first billion years, the diffuse hydrogen gas between galaxies transitioned from a neutral to an ionised state – a process called reionisation. Observations of the cosmic microwave background suggest the mid-point of reionisation occurred around redshift $z \approx 7.5$ (Planck Collaboration et al. 2020; Gorce et al. 2022), although this only gives an integral constraint on the timing. A wide range of other observables suggest reionisation finished at $z < 6$, and perhaps even as late as $z \approx 5.3$: the distribution of the Lyman α (Ly α) forest effective optical depth (Bosman et al. 2022); the rapid evolution of the mean free path of Lyman limit photons around $z \sim 6$ (Becker et al. 2021; Zhu et al. 2023; Satyavolu et al. 2024); observations of damping wings in the spectra of $z \lesssim 6$ quasars (Becker et al. 2024; Spina et al. 2024; Zhu et al. 2024); and the incidence of dark gaps in the Ly α forest (McGreer et al. 2015; Jin et al. 2023; Davies et al. 2026). However, while there has been great progress in constraining the timing of the end of reionisation, the nature of the ionising sources remains an open question.

A promising avenue for gaining insight into the sources driving reionisation is the correlation of high-redshift galaxies with Ly α forest transmission (e.g. Kakiichi et al.

2018; Meyer et al. 2019, 2020). The advent of *JWST* has enabled surveys of [O III]-emitting galaxies in fields around bright quasars, opening up a new window into this correlation during the second half of reionisation (Kashino et al. 2023; Kakiichi et al. 2025; Kashino et al. 2026; Zhu et al. 2026). The [O III] line is targeted because it allows a clear determination of redshift, while also being sensitive to the ionising photon production of galaxies (e.g. Wilkins et al. 2023). Large-scale surveys such as FRESCO (Meyer et al. 2024) and COSMOS-3D (Meyer et al. 2025) are targeting the [O III] $\lambda\lambda 4960, 5008$ emission line over large areas, while smaller-scale surveys are focused on the fields of high-redshift quasars. In the latter category, EIGER (Kashino et al. 2023) and ASPIRE (Wang et al. 2023) are carried out using the wide-field slitless spectroscopic mode of *JWST*'s NIR-Cam. The survey designs range from single pointings in the case of ASPIRE to more complex mosaicked tilings in the case of EIGER.

The latest observations of the [O III] emitter–Ly α cross correlation point to an excess in intergalactic Ly α transmission relative to the mean at scales of ~ 10 – 40 cMpc from galaxies (Kakiichi et al. 2025; Kashino et al. 2026). The signature is driven largely by enhanced ionisation around the galaxies, with temperature fluctuations due to inhomogeneous reionisation playing a secondary role (Conaboy et al. 2025). A range of theoretical models

*E-mail: luke.conaboy@nottingham.ac.uk

also predict this reported excess (Garaldi et al. 2022, 2025a; Conaboy et al. 2025; Basu et al. 2026, but see also Garaldi et al. 2019; Zhu et al. 2024), although the observed scale and amplitude are challenging to reproduce. Recently, Zhu et al. (2026) have also carried out the first analysis of the two-dimensional cross-correlation between *JWST*-detected [O III] emitters and Ly α transmission in the field of two high-redshift quasars, finding possible evidence for the anisotropic escape of ionising photons.

However, the modelling of the cross-correlation has not always considered the detailed properties of the [O III] emitter population or the impact of NIRCcam field-of-view and survey depth (with the recent notable exception of Garaldi et al. 2025a). In this context, we extend our earlier work using the Sherwood-Relics simulations (Conaboy et al. 2025), in which the [O III] emitters were assigned to dark matter haloes using a cut in halo mass with $M_h \geq 10^{10} h^{-1} M_\odot$. Using this simple approach, Conaboy et al. (2025) found reasonable quantitative agreement ($< 1.5\sigma$) with the ASPIRE cross-correlation results presented in Kakiichi et al. (2025), but with a peak in the correlation that occurred at scales ~ 10 cMpc below that observed. Here we develop a more detailed empirical model to connect the haloes in our simulation with the population of [O III] emitters observed by *JWST*. We then quantify the impact of this updated approach on the shape of the galaxy–Ly α transmission correlation. Finally, we apply this model to the latest observations of the Ly α forest opacity and galaxy density relation using [O III]-selected galaxies (Zhu et al. 2026).

Throughout this paper we assume a flat Λ CDM cosmology with $\Omega_\Lambda = 0.692$, $\Omega_m = 0.308$, $\Omega_b = 0.0482$, $\sigma_8 = 0.829$, $n_s = 0.961$ and $h = 0.678$ (Planck Collaboration et al. 2014). Unless otherwise specified, distance units are comoving (and may be explicitly specified as such by the prefix ‘c’). Magnitudes are quoted in the AB system (Oke & Gunn 1983).

2. MODEL

2.1. The Sherwood-Relics simulations

The Sherwood-Relics simulation suite (Puchwein et al. 2023) is a set of high-resolution cosmological hydrodynamical simulations performed with a modified version of the P-GADGET-3 code (itself a modified version of GADGET-2, described in Springel 2005). Here we use the 236 cMpc (i.e. $160 h^{-1}$ cMpc) box, containing 2×2048^3 particles, with a dark matter particle mass of $M_d = 5.07 \times 10^7 M_\odot$ and a gas particle mass of $M_g = 9.41 \times 10^6 M_\odot$. The simulation suite is primarily focused on studying the intergalactic medium (IGM) and does not include any subgrid prescription for galaxy formation. It instead employs a computationally-efficient scheme to remove dense gas, converting all gas particles with overdensity $\rho_g/\bar{\rho}_g = \Delta > 1000$ and temperature $T < 10^5$ K to collisionless star particles (the ‘quick Ly α ’ approach, Viel et al. 2004). Halo finding is performed using the inbuilt friends-of-friends (FoF) halo finder (Springel 2005), with the standard linking length of 0.2 times the mean interparticle spacing. Note that whenever we discuss ‘halo mass’, we refer to total FoF group mass $M_h = M_{h,d} + M_{h,g} + M_{h,*}$ where $M_{h,d}$, $M_{h,g}$, and $M_{h,*}$ are the dark matter, gas and stellar mass com-

ponents of the halo, respectively.

Sherwood-Relics uses a novel hybrid radiative transfer scheme to capture the hydrodynamical effect of patchy reionisation, as discussed in detail in Puchwein et al. (2023). The luminosity of each source is proportional to its halo mass, and the minimum mass of haloes that host ionising sources is $M_h > 10^{9.17} M_\odot$ (i.e. $> 10^9 h^{-1} M_\odot$). The emissivity of each halo is determined by fixing the redshift evolution of the global emissivity, with the latter calibrated to match the observed Ly α forest transmission (Kulkarni et al. 2019; Keating et al. 2020a). The simulation used in this work completes reionisation at $z = 5.3$ and is matched to the Bosman et al. (2022) mean Ly α transmission constraints (see fig. 1 in Conaboy et al. 2025).

Sightlines are drawn through the simulation volume with a spatial resolution of 115.2 ckpc to obtain the quantities needed to produce mock Ly α absorption spectra. The Ly α optical depths are computed using the Tepper-García (2006) approximation to the Voigt line profile, including the effects of peculiar velocities.

2.2. Populating haloes with [O III] emitters

In order to relate the haloes in the Sherwood-Relics simulation to galaxies, we construct an empirical relation between halo mass and observed galaxy properties. We achieve this by using the abundance matching technique (Vale & Ostriker 2004; Cooray & Milosavljević 2005) to populate haloes with [O III]-emitting galaxies, an approach that has already been widely applied to high redshift galaxies (e.g. Bouwens et al. 2008; Lee et al. 2009; Trenti et al. 2010; Trac et al. 2015).

We shall first abundance match the halo mass function of our simulation to the observed UV luminosity function, before using a scaling relation to obtain the [O III] luminosity. We choose to abundance match to the UV luminosity function and convert to [O III] luminosities – as opposed to matching directly the [O III] luminosity function – as the UV luminosity function at $z \sim 6$ has been well constrained using deep and wide *HST* observations (Bouwens et al. 2021). This contrasts with the small survey area and limited sample size of current [O III] emitter surveys carried out with *JWST* (Matthee et al. 2023, although see also Meyer et al. 2025 for a large *JWST* survey at $z \sim 7$).

2.2.1. Abundance matching

We relate UV luminosities to halo masses by assuming that the abundance of objects measured by each tracer should be equal, i.e.

$$\int_{L_{UV}}^{\infty} \phi(L'_{UV}, z) dL'_{UV} = \epsilon_{DC}(M_h, z) \int_{M_h}^{\infty} n(M'_h, z) dM'_h, \quad (1)$$

where L_{UV} is the UV luminosity, $\phi(L_{UV}, z)$ is the UV luminosity function, M_h is halo mass, $n(M_h, z)$ is the differential halo mass function, and $0 \leq \epsilon_{DC}(M_h, z) \leq 1$ is the duty cycle, which in general can be mass and redshift dependent. For the UV luminosity function, we use the Schechter function fit in Bouwens et al. (2021),

which is presented in magnitude form as

$$\phi(M_{\text{UV}}) dM_{\text{UV}} = 0.4 \ln 10 \phi^* \left[10^{-0.4(M_{\text{UV}} - M_{\text{UV}}^*)} \right]^{\alpha+1} \times \exp \left[-10^{-0.4(M_{\text{UV}} - M_{\text{UV}}^*)} \right] dM_{\text{UV}}, \quad (2)$$

where ϕ^* is the normalisation of the Schechter function, M_{UV}^* is the characteristic luminosity, and α is the faint-end slope. We match to the $z = 5.9$ fit, with parameters

$$\begin{aligned} \phi^* &= 0.51_{-0.10}^{+0.12} \times 10^{-3} \text{ cMpc}^{-3}, \\ M_{\text{UV}}^* &= -20.93 \pm 0.09, \\ \alpha &= -1.93 \pm 0.08. \end{aligned} \quad (3)$$

We convert this to the Schechter function in its luminosity form

$$\phi(L_{\text{UV}}) dL_{\text{UV}} = \frac{\phi^*}{L_{\text{UV}}^*} \left(\frac{L_{\text{UV}}}{L_{\text{UV}}^*} \right)^\alpha \exp \left(-\frac{L_{\text{UV}}}{L_{\text{UV}}^*} \right) dL_{\text{UV}}, \quad (4)$$

where L_{UV}^* is the characteristic luminosity, obtained from M_{UV}^* using the definition of AB magnitude

$$M_{\text{UV}} = -2.5 \log_{10} \left(\frac{L_{\text{UV},\nu}}{\text{erg s}^{-1} \text{ Hz}^{-1}} \right) + 51.6. \quad (5)$$

Here $L_{\text{UV},\nu}$ is the monochromatic UV luminosity at 1600 Å. Note there is an analytic solution to the integral on the left-hand side of Eq. (1), $\int_{L_{\text{UV}}}^{\infty} \phi(L'_{\text{UV}}, z) dL'_{\text{UV}} = \phi^* \Gamma(\alpha + 1, L_{\text{UV}}/L_{\text{UV}}^*)$, where Γ is the upper incomplete gamma function, avoiding the need to carry out a numerical integration.

We incorporate the uncertainties on the parameters in Eq. (3) by generating 1024 draws of the luminosity function, independently sampling the uncertainties on each parameter from a Gaussian (or two half-Gaussians when the errors are asymmetric, Barlow 2003). From each of these draws of the luminosity function, we generate a mapping $L_{\text{UV}}(M_h)$ from which we can estimate the median and 68 per cent confidence intervals. The uncertainties on each parameter are not independent (cf. fig. 6 in Bouwens et al. 2021), but we do not have access to the original distribution from which the uncertainties in Eq. (3) are calculated. To account for this, we follow Trac et al. (2015) in multiplying the uncertainties on each parameter by 0.7, such that the 1σ confidence interval on $\phi(M_{\text{UV}})$ is approximately equal to the 1σ uncertainty on the binned data points from Bouwens et al. (2021).

For the differential halo mass function, $n(M_h, z)$, we use the analytic Sheth et al. (2001) halo mass function. This agrees with the halo mass function measured from our simulation to better than 10 per cent (and mostly better than 1 per cent) over the redshifts and masses we consider. Using the analytic halo mass function to construct the $L_{\text{UV}}(M_h)$ mapping – as opposed to the mass function from our simulation – has the advantage that it does not suffer from resolution or finite box size effects at the low and high-mass ends, respectively. Note that the analytic mass function is only used to construct the $L_{\text{UV}}(M_h)$ mapping, and all other results in this work use the haloes obtained from the Sherwood-Relics simulation.

Lastly, for the duty cycle we use the Trenti et al. (2010) ‘improved conditional luminosity function’, which has been demonstrated to perform well for abundance matching studies at high redshift (e.g. Weinberger et al. 2019; Keating et al. 2020b; Chakraborty & Choudhury 2026; Maitra et al. 2025). The duty cycle is defined for a halo mass M_h and at a redshift z as

$$\epsilon_{\text{DC}}(M_h, z) = \frac{\int_{M_h}^{\infty} [n(M'_h, z) - n(M'_h, z_{\Delta t})] dM'_h}{\int_{M_h}^{\infty} n(M'_h, z) dM'_h}, \quad (6)$$

where $z_{\Delta t}$ is the redshift corresponding to the time $t(z) - \Delta t$, $t(z)$ is the age of the Universe at redshift z and Δt is the timescale over which galaxies are UV bright. Trenti et al. (2010) chose $\Delta t = 200$ Myr, but in this work we choose a shorter timescale $\Delta t = 50$ Myr. Our choice of Δt is motivated by the fact that the escape fraction has been shown to fluctuate rapidly over timescales $\lesssim 100$ Myr in high-resolution studies of galaxy formation and feedback during the epoch of reionisation (Rosdahl et al. 2022). Similar timescales were used by Chakraborty & Choudhury (2026) who find good agreement with *JWST* UV luminosity functions and galaxy clustering measurements when using a timescale that varies with both redshift and halo mass, with $\Delta t \approx 45$ Myr at $z = 6$ for $10^{10} M_{\odot}$ haloes.

With a sample of galaxies with abundance matched UV magnitudes in hand, we next convert the UV magnitudes into [O III] luminosities. We follow Meyer et al. (2024) by calculating the ratio $L_{[\text{O III}]} / L_{\text{UV}}$ that maps the abundance-matched Bouwens et al. (2021) UV luminosity function to the observed Matthee et al. (2023) UV luminosity function of the [O III]-selected galaxies. Assuming a limiting flux sensitivity,

$$f_{\text{lim}} = \frac{L_{\text{lim}}}{4\pi D_L^2}, \quad (7)$$

where L_{lim} is the limiting [O III] $\lambda 5008$ luminosity and D_L the luminosity distance, we fit for the $L_{[\text{O III}]} / L_{\text{UV}}$ relation that reproduces the observed UV luminosity function of the [O III] emitters from the abundance-matched Bouwens et al. (2021) UV luminosity function. The limiting line sensitivity depends on the survey, with EIGER reporting a minimum of $0.6 \times 10^{-18} \text{ erg s}^{-1} \text{ cm}^{-2}$ for a 3σ detection (Matthee et al. 2023), while ASPIRE report a minimum of $2.0 \times 10^{-18} \text{ erg s}^{-1} \text{ cm}^{-2}$ for a 5σ detection (Wang et al. 2023). As a compromise, we adopt a limiting line sensitivity of $1.0 \times 10^{-18} \text{ erg s}^{-1} \text{ cm}^{-2}$ (the same as used in Meyer et al. 2024, who use the FRESCO survey).¹

As with Meyer et al. (2024), we assume that the ratio $L_{[\text{O III}]} / L_{\text{UV}}$ follows a Gaussian distribution with mean $\mu = \mu_0 + a (\log_{10} L_{\text{UV}} - \log_{10} L_{\text{UV},0})$, where L_{UV} and $L_{\text{UV},0}$ are both in units of L_{\odot} , and a standard deviation σ . In this model, the predicted $L_{[\text{O III}]}$ will fall below L_{lim} (defined in Eq. (7)) for some fraction of galaxies, rendering those galaxies undetected. This fraction of undetected galaxies should increase with M_{UV} to match the

¹ At $z = 6$, a limiting flux of $1.0 \times 10^{-18} \text{ erg s}^{-1} \text{ cm}^{-2}$ translates to an [O III] $\lambda 5008$ luminosity of $L_{[\text{O III}]} > 4.2 \times 10^{41} \text{ erg s}^{-1}$.

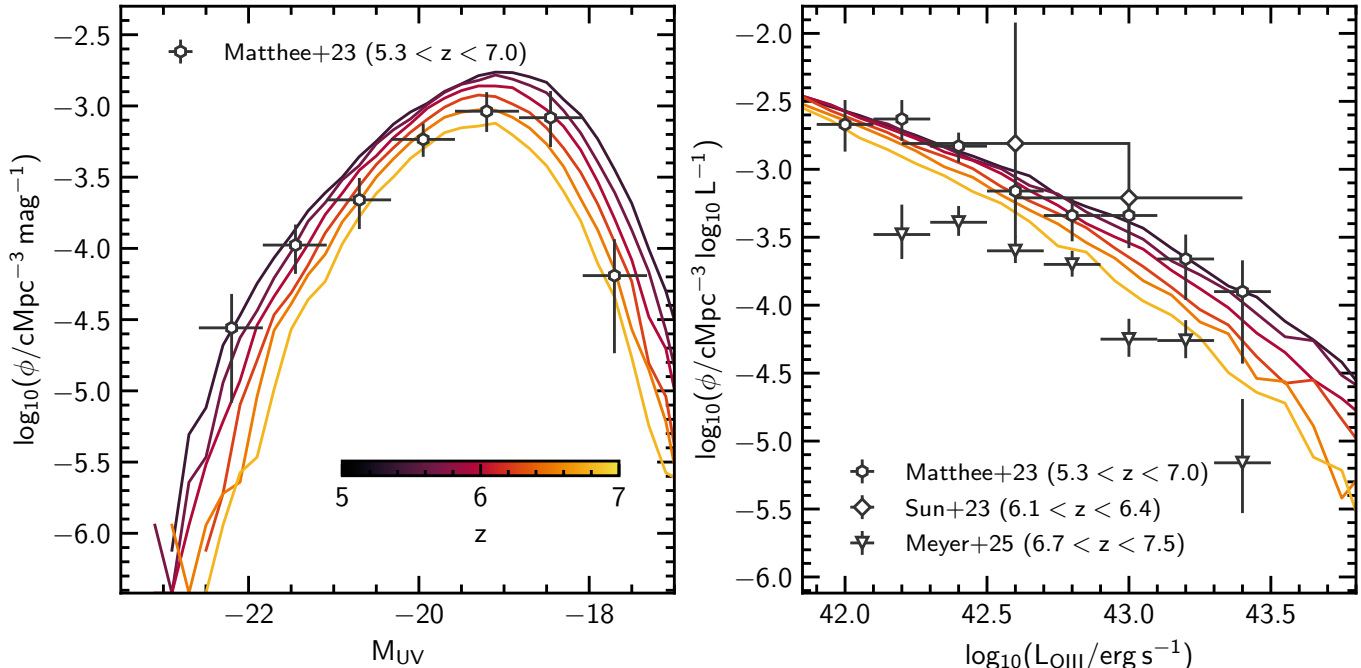


FIG. 1.— Simulated UV luminosity functions (left panel, lines), with observational data from [Matthee et al. \(2023\)](#) (grey hexagons). We also show the corresponding [O III] λ 5008 luminosity functions (right panel, lines) with observational data from [Matthee et al. \(2023\)](#) (grey hexagons), [Sun et al. \(2023\)](#) (grey diamonds), and [Meyer et al. \(2025\)](#) (grey triangles). The simulated luminosity functions are shown every $\Delta z = 0.4$ between $z = 5$ and $z = 7$, where the line colour indicates the redshift.

fall-off in the UV luminosity function of [O III]-selected galaxies at $M_{UV} \gtrsim -20$. We set $\log_{10} L_{UV,0} = 10.93$, as this is the luminosity above which the [Matthee et al. \(2023\)](#) UV luminosity function data are in best agreement with the [Bouwens et al. \(2021\)](#) UV luminosity function. Using our $z = 6$ abundance-matched UV luminosity function, we then fit for μ_0 , a , and σ using the [Matthee et al. \(2023\)](#) data to obtain the following mean $L_{[O III]}/L_{UV}$ ratio

$$\log_{10} \left(\frac{L_{[O III]}}{L_{UV}} \right) = -1.42 + 0.49 (\log_{10} L_{UV} - 10.93) \pm 0.36. \quad (8)$$

The parameter σ controls the range of $L_{[O III]}$ a given M_{UV} can take. The 68 per cent confidence interval of the fitted $\sigma = 0.36^{+0.07}_{-0.04}$, and varying σ within this range means that we are consistent with the $L_{[O III]}-M_{UV}$ relation from [Matthee et al. \(2023\)](#) for $M_{UV} \lesssim -19$, but that we predict lower [O III] luminosities for fainter magnitudes.

Using Eq. (8) we then generate [O III] λ 5008 luminosities from the UV magnitudes of the abundance matched galaxies, removing any galaxies from the catalogue with a flux that falls below the limiting line sensitivity of $1.0 \times 10^{-18} \text{ erg s}^{-1} \text{ cm}^{-2}$. After applying all of the above steps, we obtain a catalogue of [O III] emitters derived from the dark matter haloes in our simulation.

To summarise, in this work we use or compare to three types of luminosity functions:

- we first abundance match to the UV luminosity function of galaxies selected by their UV luminosity ([Bouwens et al. 2021](#));
- we then fit the UV luminosity function of galaxies selected by their [O III] λ 5008 emission ([Matthee et al. 2023](#)) using Eq. (8);

et al. 2023) using Eq. (8);

- lastly, we predict the [O III] λ 5008 luminosity function of galaxies selected by their [O III] λ 5008 emission ([Matthee et al. 2023](#), [Sun et al. 2023](#), and [Meyer et al. 2025](#)).

2.2.2. Galaxy abundance

We now present some consistency checks of our simulated galaxy catalogue. In Fig. 1 we show the UV and [O III] λ 5008 luminosity functions for our full catalogue, i.e. making no cuts to mimic survey volume, between $5 \leq z \leq 7$. In the left panel we show the UV luminosity function compared to the observed UV luminosity function at $5.33 < z < 6.96$ from [Matthee et al. \(2023\)](#), finding excellent agreement with the observed data *by construction*, particularly around $z \approx 6$. The turnover in the UV luminosity function for $M_{UV} \gtrsim -20$ is due to incompleteness at the faint end of the observed [O III] λ 5008 luminosity function and the scatter in the $L_{[O III]}/L_{UV}$ ratio, which can mean that the [O III] line for a given L_{UV} can fall below the limiting flux sensitivity, rendering the galaxy undetected. It is also worth noting here that, although we carry out the $L_{UV}(M_h)$ mapping at fixed redshift ($z = 5.9$), the simulated luminosity functions evolve with redshift. This is due to the evolution of the underlying halo mass function in the Sherwood-Relics simulation, the redshift dependence of the duty cycle (see Eq. (6)), and the redshift evolution of L_{lim} at fixed f_{lim} (see Eq. (7)).

In the right panel of Fig. 1, we show the [O III] λ 5008 luminosity function with observational estimates from [Matthee et al. \(2023\)](#), [Sun et al. \(2023\)](#) ($6.11 < z < 6.35$), and [Meyer et al. \(2025\)](#) ($6.75 < z < 7.50$). We find good agreement with [Matthee et al. \(2023\)](#), particularly at $z \lesssim 6.4$, and note that this is no longer by construc-

tion; the [O III] luminosity function from [Matthee et al. \(2023\)](#) never features in our fitting. Instead, this good agreement demonstrates the validity of the $L_{[\text{O III}]} / L_{\text{UV}}$ ratio modelling discussed in Sec. 2.2.1, as well as the consistency between the UV and [O III] luminosity functions reported by [Matthee et al. \(2023\)](#). We predict slightly lower abundances than [Sun et al. \(2023\)](#) (although still within 1σ for $z \lesssim 6.8$). However, we note that the [Sun et al. \(2023\)](#) sample comprises only four [O III] emitters. We overshoot the [Meyer et al. \(2025\)](#) measurement at all redshifts and luminosities except for the point at $\log_{10}(L_{[\text{O III}]} / \text{erg s}^{-1}) = 43.2$ and $z = 7$. This is perhaps not too surprising given that the mean redshift of the [Meyer et al. \(2025\)](#) dataset is $\langle z \rangle = 7.1$, i.e. higher than any redshift we show, and that the abundance of [O III] emitters at all luminosities tends to decrease with increasing redshift.

2.2.3. Galaxy clustering

Two *JWST* programmes, EIGER and ASPIRE, have recently reported measurements of the clustering of high-redshift, [O III]-selected galaxies ([Eilers et al. 2024](#); [Huang et al. 2026](#)). They quantify the strength of the clustering using the volume-averaged projected autocorrelation function ([Hennawi et al. 2006](#); [García-Vergara et al. 2017](#); [Eilers et al. 2024](#)),

$$\chi_V(r_{\perp, \min}, r_{\perp, \max}) = \frac{2}{V} \int_{r_{\perp, \min}}^{r_{\perp, \max}} \int_0^{Z_{\max}} \xi(r_{\perp}, Z) 2\pi r_{\perp} dr_{\perp} dZ, \quad (9)$$

where r_{\perp} is the radial distance perpendicular to the line-of-sight, Z is the line-of-sight separation, and $\xi(r_{\perp}, Z)$ is the correlation function binned in both the radial and line-of-sight directions. The volume of each cylindrical shell, V , is given by

$$V = 2Z_{\max} \pi (r_{\perp, \max}^2 - r_{\perp, \min}^2), \quad (10)$$

where Z_{\max} is the maximum line-of-sight separation.

[Eilers et al. \(2024\)](#) determine Z_{\max} through fixing the maximum velocity difference by which pairs of galaxies can be separated $v_{\max} = |\Delta v|$, giving

$$Z_{\max} = \frac{v_{\max}(1+z)}{H(z)}, \quad (11)$$

where $H(z)$ is the Hubble parameter at z , and $v_{\max} = 1000 \text{ km s}^{-1}$, corresponding to $Z_{\max} \approx 10.3 \text{ cMpc}$ (i.e. $7 h^{-1} \text{ cMpc}$) at $z = 6$. Instead, [Huang et al. \(2026\)](#) fix $Z_{\max} \approx 10.3 \text{ cMpc}$, thus implicitly allowing v_{\max} to vary with redshift. We follow [Eilers et al. \(2024\)](#), and fix $v_{\max} = 1000 \text{ km s}^{-1}$, but note that the difference should be small (e.g. [Huang et al. 2026](#) obtain $v_{\max} = 1037 \text{ km s}^{-1}$ at $z = 6.5$). When computing autocorrelation functions from the EIGER results, [Eilers et al. \(2024\)](#) include all galaxies with $\log_{10}(L_{[\text{O III}]} / \text{erg s}^{-1}) \geq 42.0$, and [Huang et al. \(2026\)](#) use a lower limit of $\log_{10}(L_{[\text{O III}]} / \text{erg s}^{-1}) > 41.8$. However, for the EIGER survey, the completeness at this luminosity is only ~ 40 per cent, rising to ~ 80 per cent for $\log_{10}(L_{[\text{O III}]} / \text{erg s}^{-1}) \geq 42.4$ ([Kashino et al. 2026](#)). For this reason, we follow [Pizzati et al. \(2024\)](#) who only

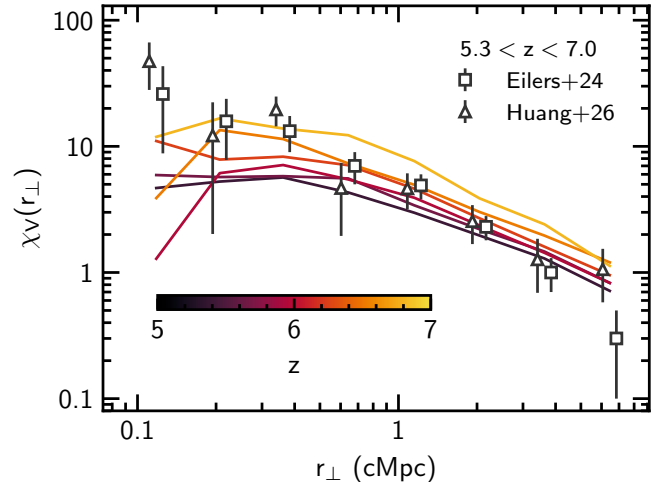


FIG. 2.— Simulated [O III] λ 5008 volume-averaged projected autocorrelation functions (solid) for all haloes in the catalogue, compared to observational results from [Eilers et al. \(2024\)](#) (grey squares) and [Huang et al. \(2026\)](#) (grey triangles), both covering the redshift range $5.3 < z < 7.0$ and using the same binning (although for clarity, we shift the [Huang et al. \(2026\)](#) points slightly left and the [Eilers et al. \(2024\)](#) points slightly right). We include all galaxies with $\log_{10}(L_{[\text{O III}]} / \text{erg s}^{-1}) > 42.4$. The line colours are the same as in Fig. 1.

include galaxies with $\log_{10}(L_{[\text{O III}]} / \text{erg s}^{-1}) \geq 42.4$ when comparing their clustering model to the EIGER observations. Making this minimum cut in luminosity yields a mean luminosity ($\log_{10}(L_{[\text{O III}]} / \text{erg s}^{-1}) = 42.73$ at $z = 6$, which is 0.20 dex larger than the mean luminosity of 42.53 reported by [Huang et al. \(2026\)](#), while a cut of $\log_{10}(L_{[\text{O III}]} / \text{erg s}^{-1}) > 41.8$ would yield a mean luminosity of 42.20, i.e. 0.33 dex smaller than [Huang et al. \(2026\)](#). To estimate autocorrelation functions from our catalogues, we use CORRFUNC ([Sinha & Garrison 2020](#)) with the Landy–Szalay estimator ([Landy & Szalay 1993](#)).

In Fig. 2 we show the volume-averaged projected autocorrelation function at $5 \leq z \leq 7$ for all galaxies with $\log_{10}(L_{[\text{O III}]} / \text{erg s}^{-1}) \geq 42.4$ in our catalogue, again making no spatial cuts to mimic the EIGER or ASPIRE surveys, along with the observational data from [Eilers et al. \(2024\)](#) (calculated for all galaxies with $\log_{10}(L_{[\text{O III}]} / \text{erg s}^{-1}) \geq 42.0$) and [Huang et al. \(2026\)](#) (calculated for all galaxies with $\log_{10}(L_{[\text{O III}]} / \text{erg s}^{-1}) > 41.8$). We find that the strength of clustering in our model generally increases across all spatial scales as redshift increases. For $z \lesssim 6.2$, we tend to find weaker clustering than [Eilers et al. \(2024\)](#) for $r_{\perp} \lesssim 0.4 \text{ cMpc}$. We predict a flatter slope of χ_V over r_{\perp} than [Eilers et al. \(2024\)](#). We find better agreement with the clustering measurements of [Huang et al. \(2026\)](#) over a range of redshifts, except at $r_{\perp} \approx 0.3 \text{ cMpc}$ where only our $z = 7$ estimate is in agreement with the data, and in the smallest radial bin at $r_{\perp} \approx 0.1 \text{ cMpc}$ where none of our estimates are in agreement.

Most noticeably, our models predict that the slope of χ_V should flatten, and even turn over, for $r_{\perp} \lesssim 0.4 \text{ cMpc}$. This is contrary to the observational estimates, which predict that χ_V should continue to rise for these small r_{\perp} . This is largely a consequence of the technique that we use to identify haloes in our simulation, FoF, which identifies haloes by linking groups of nearby particles, and so does not allow for the possibility that a dark matter

halo could host more than one galaxy. This is a well-known problem when modelling the correlation function of galaxies by populating dark matter haloes, where the phrase ‘one-halo term’ is commonly used to describe the enhanced contribution on small scales from multiple galaxies in the same dark matter halo (e.g. Cooray & Sheth 2002). We have verified that the missing clustering amplitude on small scales is indeed caused by the missing one-halo term by reanalysing one of our snapshots with ROCKSTAR (Behroozi et al. 2013), a halo finder that provides information about substructure. The χ_V calculated from this catalogue (see Sec. B) is in good agreement with the data for $r_\perp \lesssim 0.4$ cMpc.

3. GALAXY-LYMAN α TRANSMISSION CROSS-CORRELATION

The reasonable agreement between our simulated galaxy catalogue and the observed [O III] luminosity function and autocorrelation function enables us to discuss the impact of galaxy selection on the galaxy-Ly α transmission cross-correlation. In addition to the source modelling discussed in Sec. 2.2, we now additionally mimic the characteristics of the *JWST* surveys, namely, the galaxy sample (i.e. number and luminosity) and the survey geometry (i.e. field-of-view and sightline length). When designing our mock survey, we focus on the latest results from the ASPIRE survey (Kakiichi et al. 2025).

3.1. Galaxy sample

The distribution of UV magnitudes probed by the ASPIRE survey (see the red histogram on the top panel of Fig. 3) is well-fit by a Gaussian with mean $\langle M_{UV} \rangle = -19.7$ and standard deviation $\sigma_{M_{UV}} = 0.7$. For each of the five quasar sightlines in the ASPIRE survey we therefore draw [O III] emitters from this Gaussian such that the mean number of [O III] emitters in a typical ASPIRE-like realisation $\langle N_{[O III]} \rangle$ is similar to that in Kakiichi et al. (2025). At $z = 6.4, 6.0,$ and 5.6 we find $\langle N_{[O III]} \rangle = 7.2, 8.8,$ and 10.2 , compared to $\langle N_{[O III]} \rangle = 9.8$ in Kakiichi et al. (2025), although our results are not very sensitive to this choice. We have verified that performing the calculation with $\langle N_{[O III]} \rangle = 17.4$ at $z = 6$ does not change our results, consistent with the findings of Garaldi et al. (2025a) (see their fig. 5). An example of the resultant $L_{[O III]}-M_{UV}$ relation is shown in Fig. 3, along with the observed relation from Kakiichi et al. (2025) and the linear fit from Matthee et al. (2023). Note that in Fig. 3 we show the [O III] $\lambda\lambda 4960, 5008$ luminosity, as opposed to the [O III] $\lambda 5008$ luminosity used throughout the rest of this work, and relate the two using the theoretical [O III] $\lambda 4960$: [O III] $\lambda 5008$ line ratio of 1:2.98 (Storey & Zeppen 2000).

By design, our model has a similar distribution in M_{UV} to Kakiichi et al. (2025), however the galaxies tend to have slightly lower $L_{[O III]}$ than both Matthee et al. (2023) and Kakiichi et al. (2025) due to the steeper $L_{[O III]}-M_{UV}$ relation required to reproduce the [O III]-selected Matthee et al. (2023) UV luminosity function from the (abundance-matched) Bouwens et al. (2021) UV luminosity function. This leads to a mean luminosity $\langle \log_{10}(L_{[O III]}/\text{erg s}^{-1}) \rangle \approx 42.5$ in our model, compared to ≈ 42.6 in Kakiichi et al. (2025). As a consequence of the abundance matching process, the mean halo mass

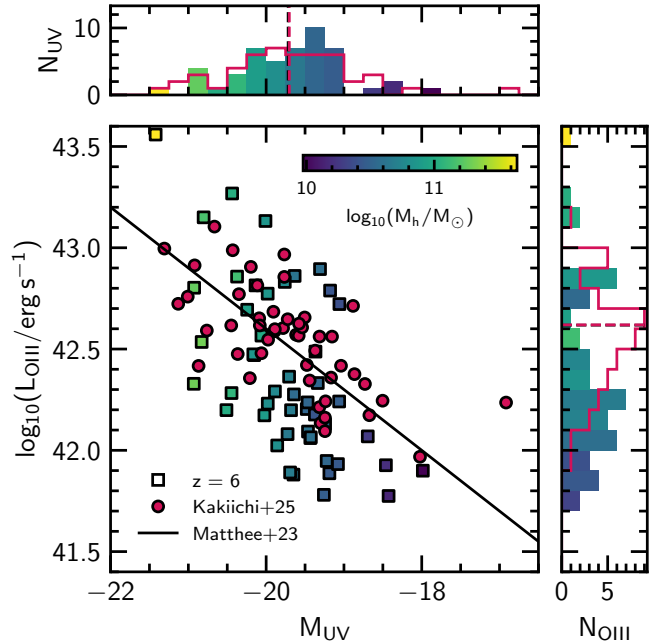


FIG. 3.— Relation between UV magnitude and [O III] $\lambda\lambda 4960, 5008$ luminosity for a single mock realisation of an ASPIRE-like survey at $z = 6$ (coloured squares), where the colour of the square shows $\log_{10}(M_h/M_\odot)$. Also shown are the observations from ASPIRE (red circles, Kakiichi et al. 2025) and the relation from Matthee et al. (2023). Side panels show the marginal distributions for ASPIRE (red line) and this work (coloured filled bars), where the colour of the filled bars shows $\langle \log_{10}(M_h/M_\odot) \rangle$ for that bin. The dashed lines indicate the means.

$\langle \log_{10}(M_h/M_\odot) \rangle$ (indicated by the colour of the points and filled bars in Fig. 3) monotonically increases with M_{UV} , but the scatter in the $L_{[O III]}/L_{UV}$ ratio means that $\langle \log_{10}(M_h/M_\odot) \rangle$ does not increase strictly monotonically with $L_{[O III]}$. However, the general trend is that galaxies brighter in $L_{[O III]}$ occupy more massive haloes. We note that the shape of the $L_{[O III]}-M_{UV}$ relation is sensitive to both the choice of f_{lim} and the redshift at which the fitting of Eq. (8) is carried out. Increasing f_{lim} tends to increase the amplitude of the $L_{[O III]}-M_{UV}$ relation, meaning that a galaxy of a given M_{UV} will tend to be brighter in $L_{[O III]}$. Holding f_{lim} fixed, but increasing the redshift at which the fit is carried out tends to result in a shallower $L_{[O III]}-M_{UV}$ relation.

3.2. Survey geometry

The ASPIRE survey employs single NIRCcam pointings, where each of the modules has an angular size of $2.2'$, with a $44''$ gap between modules. The quasar sightline is placed in Module A at an offset relative to the centre of the entire field of view (in both horizontal and vertical) of $X_{offset} = -60''.5$ and $Y_{offset} = 7''.5$ (Wang et al. 2023). This survey design is much simpler than, for example, the multi-visit strategy employed by EIGER, which leads to a complex completeness map (cf. fig. 4 in Kashino et al. 2026). We also note that the efficiency of NIRCcam’s Module B grism is ~ 30 percent of that of Module A (Greene et al. 2016), but defer a detailed study of the impact of this – if any – to future work.

The extent of the Ly α forest used by ASPIRE is ~ 450 cMpc, which is almost double our box size of 236 cMpc, and so we periodically extend the sightlines

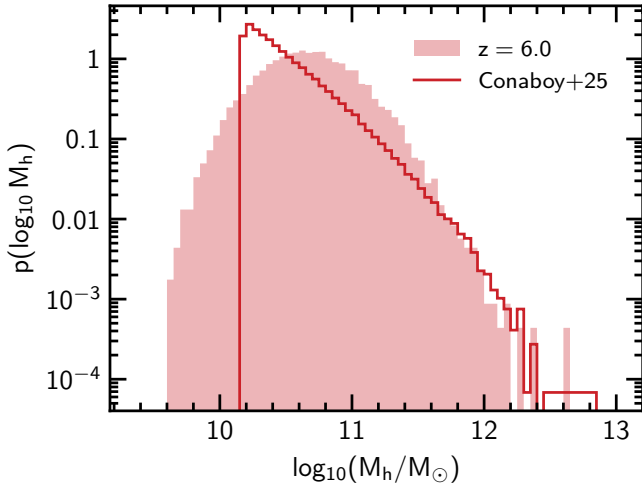


FIG. 4.— The probability distribution of halo masses used in the calculation of the [O III] emitter-Ly α cross-correlation at $z = 6$ (see Fig. 5). Filled bars indicate the distribution used in this work, while the red curve indicates the distribution used in Conaboy et al. (2025), i.e. all haloes with $M_h \geq 10^{10} h^{-1} M_\odot$.

to the required length and randomly periodically shift galaxies along the sightline to ensure uniform coverage.

3.3. Mock survey

We fold all of these observational aspects together to generate a realisation of a mock survey. We generate five quasar sightlines as in the ASPIRE programme, where each sightline used in Kakiichi et al. (2025) has the same geometric properties – sightline length and field-of-view – in our model. Given the randomness involved in generating each sightline – i.e. which sightline is chosen and which haloes from the parent catalogue are selected – we generate an ensemble of 1024 realisations of these five sightlines. Each realisation we call a ‘survey’, and from the ensemble of surveys we may obtain the mean and distribution of the cross-correlation as a function of distance from galaxies.

3.4. Results

In Fig. 4 we first show the distribution of halo masses used to calculate the galaxy-Ly α transmission correlation at $z = 6$ in Conaboy et al. (2025) and of all the 1024 mock ASPIRE-like surveys described in Sec. 3.3. We obtain a mean halo mass of $\langle \log_{10}(M_h/M_\odot) \rangle \approx 10.7$ at $z = 6$, compared to ≈ 10.5 for the sample in Conaboy et al. (2025). We find that our sample covers roughly three decades in halo mass and extends down to $\log_{10}(M_h/M_\odot) \approx 9.6$, well below the lower limit of $\log_{10}(M_h/M_\odot) \approx 10.2$ applied in Conaboy et al. (2025). The larger scatter in halo masses is attributable to the scatter intrinsic to the $L_{UV}(M_h)$ abundance matching (from the uncertainties in the Schechter fits), as well as the scatter in M_{UV} sampled by ASPIRE.

In Fig. 5 we show the cross correlation in its usual form

$$\delta_F = \frac{\langle F(r) \rangle}{\bar{F}} - 1, \quad (12)$$

where $\langle F(r) \rangle$ is the average transmission measured at a distance r from galaxies, and \bar{F} is the global mean transmission (calculated from all the sightlines available for each snapshot), for a range of redshifts bracketing

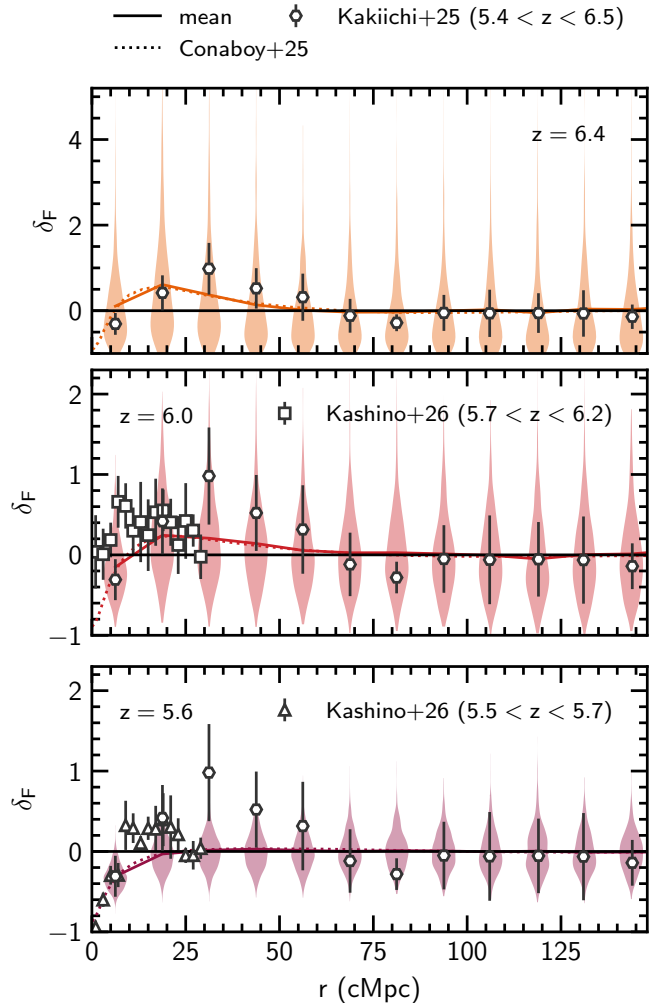


FIG. 5.— The galaxy-Ly α transmission cross correlation at $z = 6.4, 6.0$ and 5.6 (top, middle and bottom panels) for our full forward model. Solid curves indicate the mean, and the violin plots indicate the distribution of δ_F within each r bin from 1024 ASPIRE-like realisations using kernel density estimation. Note that at $z = 6.4$, some of the bins extend to larger values of δ_F than shown here but, to preserve dynamic range, we clip the long tail of these distributions and there are different δ_F ranges displayed on the top and bottom two panels. Also shown is the modelling from Conaboy et al. (2025) (calculated for all haloes with $M_h \geq 10^{10} h^{-1} M_\odot$, dotted curves) along with observational results from ASPIRE (at $5.4 < z < 6.5$, grey hexagons, Kakiichi et al. 2025) and EIGER (grey squares for $5.7 < z < 6.15$ and grey triangles for $5.5 < z < 5.7$, Kashino et al. 2026).

those probed by the ASPIRE survey. On the same figure, we show the results from Conaboy et al. (2025) – which includes all haloes with $M_h \geq 10^{10} h^{-1} M_\odot$ – along with observational results from the ASPIRE (Kakiichi et al. 2025) and EIGER surveys (Kashino et al. 2026, an update to the Kashino et al. 2023 result examined in Conaboy et al. 2025).

The most striking result of our source and survey modelling in Fig. 5 is the very large scatter in δ_F , particularly at higher z . In addition, the mean of all the realisations at all redshifts are virtually indistinguishable from Conaboy et al. (2025). One reason for this large scatter is that Ly α transmission spikes are very rare at $z = 6.4$, and so the mean transmission \bar{F} is set by a few

very transmissive pixels. These pixels are well-sampled by Conaboy et al. (2025), where all sightlines in the simulation box are used. In this work, however, a subsample of five sightlines are averaged to compute δ_F – a process which is repeated 1024 times to produce the distributions in Fig. 5. In this setup, the typical (i.e. median) mean transmission computed from the subsampled sightlines in a single realisation is ~ 90 per cent of the mean transmission in the entire box at $z = 6.4$. By $z = 6.0$ and 5.6 , the distribution in transmission is much more symmetric, and the mean transmission of a typical realisation is equal to the mean transmission of the entire box. This effect can be seen in Fig. 5, where the distributions in δ_F become more symmetric below $z = 6.4$.

Across all redshifts, the large scatter in δ_F means that all of our mock surveys are consistent with $\delta_F = 0$ at almost all r (except marginally for $r \lesssim 10$ cMpc at $z = 5.6$). The scatter means it is possible to match the large amplitude of the signal in Kakiichi et al. (2025) at $z = 6.4$ (although our models are also consistent with $\delta_F < 0$), but it is not possible to shift the location of the peak from $r \approx 20$ cMpc in our models to $r \approx 30$ cMpc in the observations. This is because the [O III] emitters in our model tend to live in only slightly more massive haloes than the mass cut used in Conaboy et al. (2025) – the average halo mass in this work is ~ 0.2 dex higher than in Conaboy et al. 2025, whereas an increase of 1–2 dex in mass would be needed to significantly shift the location of peak transmission (cf. fig. 9 in Conaboy et al. 2025). We also tend to predict a smaller value of δ_F than the Kashino et al. (2026) data, although this difference could be alleviated by assuming a slightly different evolution of the global neutral fraction (i.e. effectively shifting the Kashino et al. (2026) data points to higher redshifts, see fig. 10 in Conaboy et al. 2025). Finally, we note that our updated modelling retains good agreement with the two-point cross-correlation function of Ly α emitters (LAEs) and Lyman break galaxies with Ly α transmission spikes found by Meyer et al. (2020) (cf. fig. B1 in Conaboy et al. 2025.)

We conclude that selection cuts based on the detailed modelling of the [O III]-emitter catalogue make little impact on the shape of cross correlation with Ly α transmission, but they are critical for accurately assessing the variance in the measurements. This is consistent with Garaldi et al. (2025a) and their analysis of the THESAN simulations, where these authors find a similar shape for δ_F whether they make a cut on [O III] flux or other galaxy properties (see their fig. 9). As discussed in Conaboy et al. (2025), this strongly suggests that the relationship between halo mass, ionising photon production and the volume averaged neutral fraction in the intergalactic medium will be primarily responsible for setting the shape of δ_F , and that simulation volumes $> 160^3 h^{-3}$ cMpc³ are required to better capture the high mass end of the halo mass function.

4. RELATION BETWEEN GALAXY SURFACE DENSITY AND LYMAN α EFFECTIVE OPTICAL DEPTH

We now apply our [O III]-emitter model to studying the connection between galaxy surface density, Σ_{gal} , and the Ly α forest effective optical depth measured in $50 h^{-1}$ cMpc windows, τ_{eff}^{50} . Typically, this measurement has been performed using Ly α emitters selected in nar-

rowband surveys (Becker et al. 2018; Kashino et al. 2020; Christenson et al. 2021; Ishimoto et al. 2022; Christenson et al. 2023). However, the increasing opacity of the IGM to Ly α at high redshift makes identifying Ly α emission lines difficult. Here we focus on the recent study by Zhu et al. (2026), who perform a *JWST* survey of [O III] emitters in the fields of two high-redshift quasars.

4.1. Galaxy sample

Tiled single NIRCcam pointings are employed by Zhu et al. (2026) with similar exposure times and [O III]-emitter detection methodologies as in ASPIRE. We therefore assume the same distribution in M_{UV} used in Sec. 3.1. We also apply the [O III] $\lambda 5008$ luminosity threshold employed by Zhu et al. (2026), which only includes galaxies with $\log_{10}(L_{[\text{O III}]}) > 42.1$. Finally, we use the same technique for determining the number of [O III] emitters per sightline as in Sec. 3.1. We find that this yields a typical $\langle N_{[\text{O III}]} \rangle = 28.0$, compared to $\langle N_{[\text{O III}]} \rangle = 29.0$ in Zhu et al. (2026).

4.2. Survey geometry

The NIRCcam pointings were carried out in a 4×2 mosaic (see fig. 1 of Zhu et al. 2026), with the quasars placed at the centre. As in Sec. 3.2, we ignore any effects due to the differences in throughput between Module A and Module B of NIRCcam. The depth of each NIRCcam pointing, corresponding to the redshift interval $5.3 < z < 6.1$, is ~ 370 cMpc. As before, we periodically extend our simulated quasar sightlines to the required length and randomly periodically shift galaxies along the sightlines.

4.3. Mock survey

Combining each of these aspects, we generate 2500 realisations of each quasar sightline. Given that the length of each quasar sightline contains multiple $50 h^{-1}$ cMpc regions (the window used to calculate the effective optical depth τ_{eff}^{50}), we calculate τ_{eff}^{50} and $\Sigma_{[\text{O III}]}$ over four non-overlapping regions within each sightline.

4.4. Results

In Fig. 6 we show the relation between [O III] surface density and τ_{eff}^{50} for our mock survey at $z = 5.6$ (solid curve with 68 and 95 per cent scatter given by the shading), along with the observational constraint due to Zhu et al. (2026), as well as constraints from LAEs due to Ishimoto et al. (2022)² and Christenson et al. (2023). Note that Zhu et al. (2026) have analysed two of the sightlines studied in Christenson et al. (2023), and their result (shown as the grey star in Fig. 6) sits on top of one of the Christenson et al. (2023) sightlines. Here we have followed Zhu et al. (2026) by selecting galaxies in $28 h^{-1}$ cMpc segments at the centre of the $50 h^{-1}$ cMpc regions used to calculate τ_{eff}^{50} , and the surface densities $\Sigma_{[\text{O III}]}(r_{\perp} < 10 h^{-1}$ cMpc) and $\langle \Sigma_{[\text{O III}]} \rangle$ account for the gaps between NIRCcam modules when calculating the survey area. For comparison, we also show the surface density– τ_{eff}^{50} relation assuming that every halo with

² Note that we use the recalculated values of τ_{eff}^{50} due to Christenson et al. (2023).

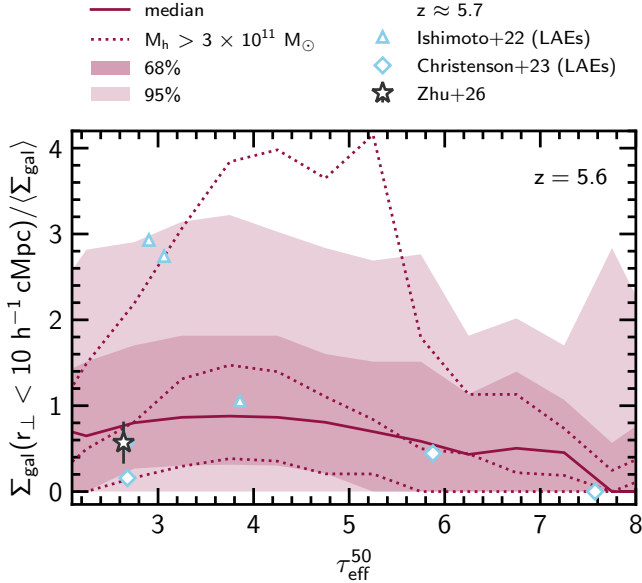


FIG. 6.— The relation between galaxy surface density and Ly α forest effective optical depth at $z = 5.6$. The galaxy surface density is measured in a $28 h^{-1} \text{cMpc}$ window, and the Ly α forest effective optical depth in a $50 h^{-1} \text{cMpc}$ window. The median relation for the mock [O III] sample is shown by the solid curve, along with the 68 per cent (dark band) and 95 per cent (light band) ranges. The dotted curves show the median and 68 per cent range for the case when all haloes with $M_h > 3 \times 10^{11} M_\odot$ are selected. This mass threshold is chosen such that $\langle \Sigma_{\text{gal}} \rangle \approx 0.02 (h^{-1} \text{cMpc})^{-2}$, matching Christenson et al. (2023). Data points show the measurements using [O III] emitters from Zhu et al. (2026) (black star) and Ly α emitters from Ishimoto et al. (2022) (blue triangles) and Christenson et al. (2023) (blue diamonds), all at $z \approx 5.7$. Note that the Zhu et al. (2026) sample comprises two of the sightlines used in the Christenson et al. (2023), one of which is directly underneath the Zhu et al. (2026) data point.

$M_h > 3 \times 10^{11} M_\odot$ hosts an [O III] emitter, which also does not account for the Zhu et al. (2026) survey geometry (dotted curves). This mass limit is chosen such that, typically, $\langle \Sigma_{\text{gal}} \rangle = 0.02 (h^{-1} \text{cMpc})^{-2}$, corresponding roughly to the typical surface density of galaxies in Christenson et al. (2023). This facilitates a fairer comparison between our model and the LAE surface densities from Ishimoto et al. (2022) and Christenson et al. (2023). In Zhu et al. (2026) the typical surface density of [O III] emitters is instead $\langle \Sigma_{\text{gal}} \rangle = 0.015\text{--}0.016 (h^{-1} \text{cMpc})^{-2}$.

Our median estimate of the galaxy density– τ_{eff}^{50} relation is in good agreement with the observational estimate from Zhu et al. (2026), although – as for Fig. 5 – there is a large scatter. Our model is able to reproduce the mean density Ishimoto et al. (2022) point at $\tau_{\text{eff}}^{50} \approx 4$, but the extreme galaxy overdensities at $\tau_{\text{eff}}^{50} \approx 3$ are at the upper end of our 95 per cent range. The results also agree well with Christenson et al. (2023) (within the 95 per cent range, and mostly within the 68 per cent range), who employ a narrowband survey to select Ly α -emitters around four $z \sim 6$ quasars. The trend of decreasing galaxy density with increasing Ly α effective optical depth – which is expected if the ionising background is stronger where the galaxy density is larger (Davies et al. 2018) – is very weak; we find that both the most transmissive ($\tau_{\text{eff}}^{50} \lesssim 3$) and most opaque ($\tau_{\text{eff}}^{50} \gtrsim 5$) sightlines in the Sherwood-Relics simulation can coincide with galaxy underdensi-

ties.

For comparison, the simpler approach based on a halo mass cut of $M_h > 3 \times 10^{11} M_\odot$ (dotted curves) gives broadly similar results to the [O III]-emitter modelling for $\tau_{\text{eff}}^{50} < 3$, and is in excellent agreement with Zhu et al. (2026). For $\tau_{\text{eff}}^{50} > 3$, it deviates from our more detailed [O III]-emitter modelling approach, most notably around $\tau_{\text{eff}}^{50} \sim 4$. These intermediate opacities are now associated with galaxy overdensities – as opposed to underdensities in the [O III]-emitter model – and the scatter is significantly larger. Overall, the simple halo mass cut leads to excellent agreement with the Christenson et al. (2023) data, as well as placing the Ishimoto et al. (2022) points at $\tau_{\text{eff}}^{50} \approx 3$ at the limit of the 68 per cent range (as opposed to the 95 per cent range), while retaining good agreement with the point at $\tau_{\text{eff}}^{50} \approx 4$. This implies that the haloes hosting the LAEs used in those studies may be more massive than the haloes hosting [O III] emitters (cf. Fig. 4). However, the large scatter in our mock survey results implies that – regardless of the halo mass selection – the late reionisation model used in Sherwood-Relics which appears to be strongly preferred by a wide range of other data (see e.g. Qin et al. 2025) remain consistent with the two-dimensional cross-correlation.

In other recent modelling work, Gangolli et al. (2025) found their FlexRT radiative transfer simulations were able to reproduce the Ishimoto et al. (2022) measurements (with the $\tau_{\text{eff}}^{50} \approx 3$ points falling just outside the 68 per cent range), as well as the Christenson et al. (2023) and Zhu et al. 2026 measurements for both transmissive and opaque sightlines. However, for their “ $N_{\text{ion}} \propto L_{\text{UV}}$ ” model at the effective optical depth of the Zhu et al. (2026) data ($\tau_{\text{eff}}^{50} \approx 2.7$), they predict a larger scatter, $0.6 \lesssim \Sigma_{\text{LAE}}(r_\perp < 10 h^{-1} \text{cMpc}) / \langle \Sigma_{\text{LAE}} \rangle \lesssim 2.4$, compared to our $0.3 \lesssim \Sigma_{[\text{O III}]}(r_\perp < 10 h^{-1} \text{cMpc}) / \langle \Sigma_{[\text{O III}]} \rangle \lesssim 1.6$. Their median galaxy density marginally favours overdense environments, whereas our results favour marginally underdense environments. Using THESAN, Garaldi et al. (2025b) are in good agreement with the Ishimoto et al. (2022) point at $\tau_{\text{eff}}^{50} \approx 3$, but they are unable to reproduce the Ishimoto et al. (2022) points at $\tau_{\text{eff}}^{50} \approx 3$. In addition, they find good agreement between the Christenson et al. (2023) data in the THESAN simulation for the transmissive sightlines at $z = 5.7$, although their models appear to undersample at $\tau_{\text{eff}}^{50} > 7$, possibly because of the smaller THESAN simulation volume ($L \approx 96 \text{cMpc}$). The preference for slight galaxy overdensities at $\tau_{\text{eff}}^{50} \approx 3$ found by both Gangolli et al. (2025) and Garaldi et al. (2025b) also suggests they consider more massive haloes in the calculation of galaxy density, closer to the halo mass cut of $M_h > 3 \times 10^{11} M_\odot$ shown in Fig. 6.

In Fig. 7 we further explore some of the model behaviour in Fig. 6, namely, that both the most transparent ($\tau_{\text{eff}}^{50} \lesssim 3$) and the most opaque ($\tau_{\text{eff}}^{50} \gtrsim 5$) sightlines exhibit the largest underdensities of galaxies. We examine this by showing in Fig. 7 the fraction of segments, $f(\tau_{\text{eff}}^{50})$, that satisfy three sets of constraints:

- where the mean overdensity over the entire segment is less than 1 (pale pink curves);
- where the mean overdensity over the entire segment

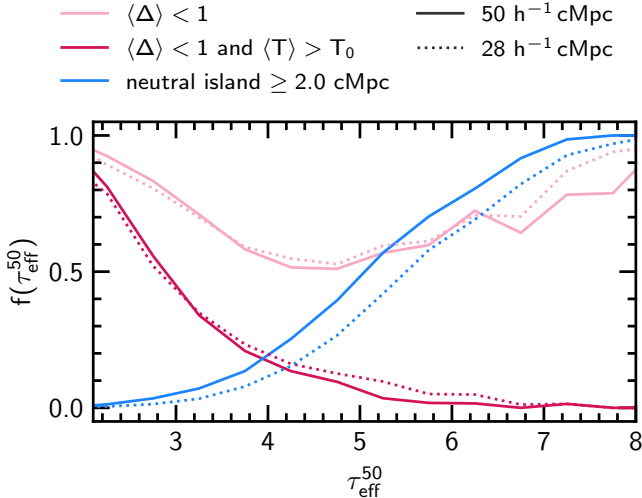


Fig. 7.— Fraction of segments in each τ_{eff}^{50} bin that are, on average, underdense ($\langle \Delta \rangle < 1$, pale pink), and both underdense and hot ($\langle T \rangle > T_0$, where T_0 is the temperature at $\Delta = 1$, pink), where the average is calculated over the entire segment. We also show the fraction of segments that contain at least one neutral island, defined as a contiguous region with $x_{\text{HI}} > 0.5$ of extent ≥ 2 cMpc (blue). The fraction represents the fraction of segments in each τ_{eff}^{50} bin. We show the fraction for segments of length $50 h^{-1}$ cMpc (i.e. the entire segment length used to calculate τ_{eff}^{50} , solid) and $28 h^{-1}$ cMpc (i.e. the central $28 h^{-1}$ cMpc corresponding the narrowband surveys of LAEs, dotted).

is less than 1 *and* the mean temperature over the entire segment is greater than the temperature at mean density, $T_0 \approx 1.2 \times 10^4$ K, at $z = 5.6$ (pink curves)

- where the segment contains at least one neutral island, defined as a contiguous region where $x_{\text{HI}} > 0.5$ for at least 2 cMpc (blue curves).

We use segments of length either $50 h^{-1}$ cMpc (corresponding to the length used to calculate τ_{eff}^{50} , solid curves), or $28 h^{-1}$ cMpc (corresponding to the narrowband region to select galaxies in the centre of the full $50 h^{-1}$ cMpc sightline, dotted curves). Both the transparent and opaque sightlines preferentially correspond to underdense environments, but the transparent sightlines typically occur in regions that are hotter than average, whereas the opaque sightlines correspond to regions that are colder than average. The fraction of segments containing neutral islands monotonically increases from $f(\tau_{\text{eff}}^{50}) \approx 0$ at $\tau_{\text{eff}}^{50} \lesssim 3$, to $f(\tau_{\text{eff}}^{50}) \approx 1$ for $\tau_{\text{eff}}^{50} \gtrsim 7$. Taken together, these results suggest that the most transparent sightlines in our model correspond to underdense regions that have recently been reionised and have not had time to cool. By contrast, the most opaque sightlines are colder and have a much higher likelihood of containing neutral islands, and likely preferentially reside in regions that are yet to be ionised.

5. CONCLUSIONS

We have examined the impact of source and survey modelling on the connection between high-redshift galaxies and Ly α forest transmission. For this purpose we use a model drawn from the Sherwood-Relics suite of simulations (Puchwein et al. 2023), which are calibrated to Ly α

forest constraints at $z \sim 6$ and are designed to capture the hydrodynamical effects of inhomogeneous reionisation on intergalactic gas. We combine this with an empirically calibrated abundance matching approach that enables us to connect haloes with the [O III]-emitting galaxies observed with *JWST*. This model is in good agreement with recent measurements of the [O III] $\lambda 5008$ luminosity function (Matthee et al. 2023; Sun et al. 2023). Our main findings are as follows:

- We find reasonable agreement ($< 1-2\sigma$) with the clustering of [O III] emitters recently reported in Huang et al. (2026) and Eilers et al. (2024), but for a slightly larger minimum luminosity $\log_{10}(L_{[\text{O III}]}/\text{erg s}^{-1}) > 42.4$ than used by those authors. We justify adopting this larger threshold because the completeness in Eilers et al. (2024) at $\log_{10}(L_{[\text{O III}]}/\text{erg s}^{-1}) = 42.0$ is 40 per cent, which rises to 80 per cent at $\log_{10}(L_{[\text{O III}]}/\text{erg s}^{-1}) = 42.4$ (see also Pizzati et al. 2024). Any differences between our model and the observations at $r_{\perp} \lesssim 0.4$ cMpc are primarily due to the missing one-halo term in our simulation group catalogues.
- We carefully forward model the survey geometry and source selection used for recent measurements of the one and two dimensional cross-correlation of [O III] emitters with the Ly α forest transmission (Kakiichi et al. 2025; Zhu et al. 2026). We find that this leads to a slight increase in the average host halo mass ($\langle \log_{10}(M_h/M_{\odot}) \rangle = 10.7$) in our models of the galaxy-Ly α transmission correlation compared the simpler approach adopted in our earlier work in Conaboy et al. (2025) ($\langle \log_{10}(M_h/M_{\odot}) \rangle = 10.5$). However, this does not change the location or magnitude of the observed excess in the one dimensional cross-correlation in our models, which peaks at scales of ~ 30 cMpc in the observational data and ~ 20 cMpc in the Sherwood-Relics simulations.
- Our more detailed modelling of the source selection also produces a very large scatter in our mock measurements of the cross-correlation. It is therefore possible to achieve a statistically good match to the observational data regardless of current differences in the predicted and observed shape of the cross-correlation. This implies that, at present, current galaxy-IGM observations may struggle to rule out a broad range of ionising source models.
- We find good statistical agreement with the latest measurement of the two-dimensional cross-correlation describing the relationship between galaxy surface density and Ly α transmission (Zhu et al. 2026). Furthermore, in agreement with recent theoretical work by Gangoli et al. (2025), we find galaxy underdensities can be associated with both the most transparent and most opaque Ly α forest sightlines. This suggests that the relationship between galaxies and gas at the tail-end of reionisation is more complex than a simple model – where the ionisation level of the intergalactic gas scales proportionally with the galaxy density – might im-

ply. We show that in our model the most transparent sightlines tend to be underdense and hotter than average, while the most opaque sightlines are more likely to correspond to regions that have yet to be fully ionised and may contain at least one neutral island.

found at <https://www.nottingham.ac.uk/astronomy/sherwood-relics/>.

We conclude that further theoretical progress will benefit from simulations performed in larger volumes, and with a wider range of source models including faint active galactic nuclei (e.g. [Asthana et al. 2025](#)). On the observational front, ongoing observational programmes such as EIGER ([Kashino et al. 2023](#)) and ASPIRE ([Wang et al. 2023](#)) that will increase sample sizes will be vital for further improving our ability to constrain models of reionisation with the galaxy-IGM connection.

ACKNOWLEDGEMENTS

LC thanks Koki Kakiichi for sharing the UV magnitudes and [O III] luminosities for the ASPIRE sample, Daichi Kashino for sharing the latest EIGER measurements of the galaxy–Ly α transmission correlation, and Christopher Lovell, Aswin Vijayan, and Romain Meyer for insightful conversations. The simulations used in this work were performed using the Joliot Curie supercomputer at the Très Grand Centre de Calcul (TGCC) and the Cambridge Service for Data Driven Discovery (CSD3), part of which is operated by the University of Cambridge Research Computing on behalf of the STFC DiRAC HPC Facility (www.dirac.ac.uk). We acknowledge the Partnership for Advanced Computing in Europe (PRACE) for awarding us time on Joliot Curie in the 16th call. The DiRAC component of CSD3 was funded by BEIS capital funding via STFC capital grants ST/P002307/1 and ST/R002452/1 and STFC operations grant ST/R00689X/1. This work also used the DiRAC@Durham facility managed by the Institute for Computational Cosmology on behalf of the STFC DiRAC HPC Facility. The equipment was funded by BEIS capital funding via STFC capital grants ST/P002293/1 and ST/R002371/1, Durham University and STFC operations grant ST/R000832/1. DiRAC is part of the National e-Infrastructure. LC and JSB are supported by STFC consolidated grant ST/X000982/1. LK acknowledges the support of a Royal Society University Research Fellowship (grant number URF\R1\251793). Support by ERC Advanced Grant 320596 ‘The Emergence of Structure During the Epoch of Reionization’ is gratefully acknowledged. MGH has been supported by STFC consolidated grants ST/N000927/1 and ST/S000623/1. We thank Volker Springel for making P-GADGET-3 available. We also thank Dominique Aubert for sharing the ATON code, and Philip Parry for technical support. This work made use of the following open-source software packages: CMASHER ([van der Velden 2020](#)); MATPLOTLIB ([Hunter 2007](#)); NUMPY ([Harris et al. 2020](#)); HMF [Murray et al. \(2013\)](#); SCIPY ([Virtanen et al. 2020](#)); and MPMATH ([The mpmath development team 2023](#)).

DATA AVAILABILITY

All data and analysis code used in this work are available from the first author on reasonable request. Further guidance on accessing the fully publicly available Sherwood-Relics simulation data may also be

REFERENCES

- Asthana, S., Haehnelt, M. G., Kulkarni, G., et al. 2025, *Monthly Notices of the Royal Astronomical Society*, 542, 2968, doi: [10.1093/mnras/staf1387](https://doi.org/10.1093/mnras/staf1387)
- Barlow, R. 2003, *Asymmetric Errors*, eprint: arXiv:physics/0401042; arXiv, doi: [10.48550/arXiv.physics/0401042](https://doi.org/10.48550/arXiv.physics/0401042)
- Basu, A., Ciardi, B., Bolton, J. S., Viel, M., & Garaldi, E. 2026, *Monthly Notices of the Royal Astronomical Society*, 546, stag174, doi: [10.1093/mnras/stag174](https://doi.org/10.1093/mnras/stag174)
- Becker, G. D., Bolton, J. S., Zhu, Y., & Hashemi, S. 2024, *Monthly Notices of the Royal Astronomical Society*, 533, 1525, doi: [10.1093/mnras/stae1918](https://doi.org/10.1093/mnras/stae1918)
- Becker, G. D., D'Aloisio, A., Christenson, H. M., et al. 2021, *Monthly Notices of the Royal Astronomical Society*, 508, 1853, doi: [10.1093/mnras/stab2696](https://doi.org/10.1093/mnras/stab2696)
- Becker, G. D., Davies, F. B., Furlanetto, S. R., et al. 2018, *The Astrophysical Journal*, 863, 92, doi: [10.3847/1538-4357/aacc73](https://doi.org/10.3847/1538-4357/aacc73)
- Behroozi, P. S., Wechsler, R. H., & Wu, H.-Y. 2013, *The Astrophysical Journal*, 762, 109, doi: [10.1088/0004-637X/762/2/109](https://doi.org/10.1088/0004-637X/762/2/109)
- Bosman, S. E. I., Davies, F. B., Becker, G. D., et al. 2022, *Monthly Notices of the Royal Astronomical Society*, 514, 55, doi: [10.1093/mnras/stac1046](https://doi.org/10.1093/mnras/stac1046)
- Bouwens, R. J., Illingworth, G. D., Franx, M., & Ford, H. 2008, *The Astrophysical Journal*, 686, 230, doi: [10.1086/590103](https://doi.org/10.1086/590103)
- Bouwens, R. J., Oesch, P. A., Stefanon, M., et al. 2021, *The Astrophysical Journal*, 162, 47, doi: [10.3847/1538-3881/abf83e](https://doi.org/10.3847/1538-3881/abf83e)
- Chakraborty, A., & Choudhury, T. R. 2026, *Journal of Cosmology and Astroparticle Physics*, 2026, 008, doi: [10.1088/1475-7516/2026/01/008](https://doi.org/10.1088/1475-7516/2026/01/008)
- Christenson, H. M., Becker, G. D., Furlanetto, S. R., et al. 2021, *The Astrophysical Journal*, 923, 87, doi: [10.3847/1538-4357/ac2a34](https://doi.org/10.3847/1538-4357/ac2a34)
- Christenson, H. M., Becker, G. D., D'Aloisio, A., et al. 2023, *The Astrophysical Journal*, 955, 138, doi: [10.3847/1538-4357/acf450](https://doi.org/10.3847/1538-4357/acf450)
- Conaboy, L., Bolton, J. S., Keating, L. C., et al. 2025, *Monthly Notices of the Royal Astronomical Society*, 539, 2790, doi: [10.1093/mnras/staf648](https://doi.org/10.1093/mnras/staf648)
- Cooray, A., & Milosavljević, M. 2005, *The Astrophysical Journal*, 627, L89, doi: [10.1086/432259](https://doi.org/10.1086/432259)
- Cooray, A., & Sheth, R. 2002, *Physics Reports*, 372, 1, doi: [10.1016/S0370-1573\(02\)00276-4](https://doi.org/10.1016/S0370-1573(02)00276-4)
- Davies, F. B., Hennawi, J. F., Bañados, E., et al. 2018, *The Astrophysical Journal*, 864, 142, doi: [10.3847/1538-4357/aad6dc](https://doi.org/10.3847/1538-4357/aad6dc)
- Davies, F. B., Bosman, S. E. I., D'Odorico, V., et al. 2026, *Monthly Notices of the Royal Astronomical Society*, 545, staf1862, doi: [10.1093/mnras/staf1862](https://doi.org/10.1093/mnras/staf1862)
- Eilers, A.-C., Mackenzie, R., Pizzati, E., et al. 2024, *The Astrophysical Journal*, 974, 275, doi: [10.3847/1538-4357/ad778b](https://doi.org/10.3847/1538-4357/ad778b)
- Gangoli, N., D'Aloisio, A., Cain, C., Becker, G. D., & Christenson, H. 2025, *Journal of Cosmology and Astroparticle Physics*, 2025, 069, doi: [10.1088/1475-7516/2025/03/069](https://doi.org/10.1088/1475-7516/2025/03/069)
- Garaldi, E., Bellscheidt, V., Smith, A., & Kannan, R. 2025a, *The Open Journal of Astrophysics*, 8, 51666, doi: [10.33232/001c.151666](https://doi.org/10.33232/001c.151666)
- . 2025b, *The Open Journal of Astrophysics*, 8, 116, doi: [10.33232/001c.143245](https://doi.org/10.33232/001c.143245)
- Garaldi, E., Gnedin, N. Y., & Madau, P. 2019, *The Astrophysical Journal*, 876, 31, doi: [10.3847/1538-4357/ab12dc](https://doi.org/10.3847/1538-4357/ab12dc)
- Garaldi, E., Kannan, R., Smith, A., et al. 2022, *Monthly Notices of the Royal Astronomical Society*, 512, 4909, doi: [10.1093/mnras/stac257](https://doi.org/10.1093/mnras/stac257)
- García-Vergara, C., Hennawi, J. F., Barrientos, L. F., & Rix, H.-W. 2017, *The Astrophysical Journal*, 848, 7, doi: [10.3847/1538-4357/aa8b69](https://doi.org/10.3847/1538-4357/aa8b69)
- Gorce, A., Douspis, M., & Salvati, L. 2022, *Astronomy and Astrophysics*, 662, A122, doi: [10.1051/0004-6361/202243351](https://doi.org/10.1051/0004-6361/202243351)
- Greene, T. P., Chu, L., Egami, E., et al. 2016, in *Space Telescopes and Instrumentation 2016: Optical, Infrared, and Millimeter Wave*, Vol. 9904, eprint: arXiv:1606.04161, 99040E, doi: [10.1117/12.2231347](https://doi.org/10.1117/12.2231347)
- Harris, C. R., Millman, K. J., van der Walt, S. J., et al. 2020, *Nature*, 585, 357, doi: [10.1038/s41586-020-2649-2](https://doi.org/10.1038/s41586-020-2649-2)
- Hennawi, J. F., Strauss, M. A., Oguri, M., et al. 2006, *The Astrophysical Journal*, 131, 1, doi: [10.1086/498235](https://doi.org/10.1086/498235)
- Huang, J., Hennawi, J., Pizzati, E., et al. 2026, *Clustering of Z₇ 6.6 Quasars and [O III] Emitters Constrains Host Halo Masses and Duty Cycles in 25 ASPIRE Fields*, arXiv, doi: [10.48550/arXiv.2602.04974](https://doi.org/10.48550/arXiv.2602.04974)
- Hunter, J. D. 2007, *Computing in Science and Engineering*, 9, 90, doi: [10.1109/MCSE.2007.55](https://doi.org/10.1109/MCSE.2007.55)
- Ishimoto, R., Kashikawa, N., Kashino, D., et al. 2022, *Monthly Notices of the Royal Astronomical Society*, 515, 5914, doi: [10.1093/mnras/stac1972](https://doi.org/10.1093/mnras/stac1972)
- Jin, X., Yang, J., Fan, X., et al. 2023, *The Astrophysical Journal*, 942, 59, doi: [10.3847/1538-4357/aca678](https://doi.org/10.3847/1538-4357/aca678)
- Kakiichi, K., Ellis, R. S., Laporte, N., et al. 2018, *Monthly Notices of the Royal Astronomical Society*, 479, 43, doi: [10.1093/mnras/sty1318](https://doi.org/10.1093/mnras/sty1318)
- Kakiichi, K., Jin, X., Wang, F., et al. 2025, arXiv e-prints, arXiv:2503.07074, doi: [10.48550/arXiv.2503.07074](https://doi.org/10.48550/arXiv.2503.07074)
- Kashino, D., Lilly, S. J., Matthee, J., et al. 2023, *The Astrophysical Journal*, 950, 66, doi: [10.3847/1538-4357/acc588](https://doi.org/10.3847/1538-4357/acc588)
- Kashino, D., Lilly, S. J., Shibuya, T., Ouchi, M., & Kashikawa, N. 2020, *The Astrophysical Journal*, 888, 6, doi: [10.3847/1538-4357/ab5a7d](https://doi.org/10.3847/1538-4357/ab5a7d)
- Kashino, D., Lilly, S. J., Matthee, J., et al. 2026, *The Astrophysical Journal*, 997, 280, doi: [10.3847/1538-4357/ae2799](https://doi.org/10.3847/1538-4357/ae2799)
- Keating, L. C., Kulkarni, G., Haehnelt, M. G., Chardin, J., & Aubert, D. 2020a, *Monthly Notices of the Royal Astronomical Society*, 497, 906, doi: [10.1093/mnras/staa1909](https://doi.org/10.1093/mnras/staa1909)
- Keating, L. C., Weinberger, L. H., Kulkarni, G., et al. 2020b, *Monthly Notices of the Royal Astronomical Society*, 491, 1736, doi: [10.1093/mnras/stz3083](https://doi.org/10.1093/mnras/stz3083)
- Kulkarni, G., Keating, L. C., Haehnelt, M. G., et al. 2019, *Monthly Notices of the Royal Astronomical Society*, 485, L24, doi: [10.1093/mnras/1/slz025](https://doi.org/10.1093/mnras/1/slz025)
- Landy, S. D., & Szalay, A. S. 1993, *The Astrophysical Journal*, 412, 64, doi: [10.1086/172900](https://doi.org/10.1086/172900)
- Lee, K.-S., Giavalisco, M., Conroy, C., et al. 2009, *The Astrophysical Journal*, 695, 368, doi: [10.1088/0004-637X/695/1/368](https://doi.org/10.1088/0004-637X/695/1/368)
- Maitra, S., Kulkarni, G., Asthana, S., et al. 2025, *Monthly Notices of the Royal Astronomical Society*, 542, 486, doi: [10.1093/mnras/staf1262](https://doi.org/10.1093/mnras/staf1262)
- Matthee, J., Mackenzie, R., Simcoe, R. A., et al. 2023, *The Astrophysical Journal*, 950, 67, doi: [10.3847/1538-4357/acc846](https://doi.org/10.3847/1538-4357/acc846)
- McGreer, I. D., Mesinger, A., & D'Odorico, V. 2015, *Monthly Notices of the Royal Astronomical Society*, 447, 499, doi: [10.1093/mnras/stu2449](https://doi.org/10.1093/mnras/stu2449)
- Meyer, R. A., Bosman, S. E. I., Kakiichi, K., & Ellis, R. S. 2019, *Monthly Notices of the Royal Astronomical Society*, 483, 19, doi: [10.1093/mnras/sty2954](https://doi.org/10.1093/mnras/sty2954)
- Meyer, R. A., Kakiichi, K., Bosman, S. E. I., et al. 2020, *Monthly Notices of the Royal Astronomical Society*, 494, 1560, doi: [10.1093/mnras/staa746](https://doi.org/10.1093/mnras/staa746)
- Meyer, R. A., Oesch, P. A., Giovinazzo, E., et al. 2024, *Monthly Notices of the Royal Astronomical Society*, 535, 1067, doi: [10.1093/mnras/stae2353](https://doi.org/10.1093/mnras/stae2353)
- Meyer, R. A., Wang, F., Kakiichi, K., et al. 2025, *JWST COSMOS-3D: Spectroscopic Census and Luminosity Function of [O III] Emitters at 6.75*, arXiv, doi: [10.48550/arXiv.2510.11373](https://doi.org/10.48550/arXiv.2510.11373)
- Murray, S. G., Power, C., & Robotham, A. S. G. 2013, *Astronomy and Computing*, 3, 23, doi: [10.1016/j.ascom.2013.11.001](https://doi.org/10.1016/j.ascom.2013.11.001)
- Oke, J. B., & Gunn, J. E. 1983, *The Astrophysical Journal*, 266, 713, doi: [10.1086/160817](https://doi.org/10.1086/160817)
- Pizzati, E., Hennawi, J. F., Schaye, J., et al. 2024, *Monthly Notices of the Royal Astronomical Society*, 534, 3155, doi: [10.1093/mnras/stae2307](https://doi.org/10.1093/mnras/stae2307)
- Planck Collaboration, Ade, P. A. R., Aghanim, N., et al. 2014, *Astronomy & Astrophysics*, 571, A16, doi: [10.1051/0004-6361/201321591](https://doi.org/10.1051/0004-6361/201321591)

Planck Collaboration, Aghanim, N., Akrami, Y., et al. 2020, *Astronomy & Astrophysics*, 641, A6, doi: [10.1051/0004-6361/201833910](https://doi.org/10.1051/0004-6361/201833910)

Puchwein, E., Bolton, J. S., Keating, L. C., et al. 2023, *Monthly Notices of the Royal Astronomical Society*, 519, 6162, doi: [10.1093/mnras/stac3761](https://doi.org/10.1093/mnras/stac3761)

Qin, Y., Mesinger, A., Prelogović, D., et al. 2025, *Publications of the Astronomical Society of Australia*, 42, e049, doi: [10.1017/pasa.2025.35](https://doi.org/10.1017/pasa.2025.35)

Rosdahl, J., Blaizot, J., Katz, H., et al. 2022, *Monthly Notices of the Royal Astronomical Society*, 515, 2386, doi: [10.1093/mnras/stac1942](https://doi.org/10.1093/mnras/stac1942)

Satyavolu, S., Kulkarni, G., Keating, L. C., & Haehnelt, M. G. 2024, *Monthly Notices of the Royal Astronomical Society*, 533, 676, doi: [10.1093/mnras/stae1717](https://doi.org/10.1093/mnras/stae1717)

Sheth, R. K., Mo, H. J., & Tormen, G. 2001, *Monthly Notices of the Royal Astronomical Society*, 323, 1, doi: [10.1046/j.1365-8711.2001.04006.x](https://doi.org/10.1046/j.1365-8711.2001.04006.x)

Sinha, M., & Garrison, L. H. 2020, *Monthly Notices of the Royal Astronomical Society*, 491, 3022, doi: [10.1093/mnras/stz3157](https://doi.org/10.1093/mnras/stz3157)

Spina, B., Bosman, S. E. I., Davies, F. B., Gaikwad, P., & Zhu, Y. 2024, *Astronomy and Astrophysics*, 688, L26, doi: [10.1051/0004-6361/202450798](https://doi.org/10.1051/0004-6361/202450798)

Springel, V. 2005, *Monthly Notices of the Royal Astronomical Society*, 364, 1105, doi: [10.1111/j.1365-2966.2005.09655.x](https://doi.org/10.1111/j.1365-2966.2005.09655.x)

Storey, P. J., & Zeppen, C. J. 2000, *Monthly Notices of the Royal Astronomical Society*, 312, 813, doi: [10.1046/j.1365-8711.2000.03184.x](https://doi.org/10.1046/j.1365-8711.2000.03184.x)

Sun, F., Egami, E., Pirzkal, N., et al. 2023, *The Astrophysical Journal*, 953, 53, doi: [10.3847/1538-4357/acd53c](https://doi.org/10.3847/1538-4357/acd53c)

Tepper-García, T. 2006, *Monthly Notices of the Royal Astronomical Society*, 369, 2025, doi: [10.1111/j.1365-2966.2006.10450.x](https://doi.org/10.1111/j.1365-2966.2006.10450.x)

The mpmath development team. 2023, *Mpmath: A Python Library for Arbitrary-Precision Floating-Point Arithmetic* (Version 1.3.0)

Trac, H., Cen, R., & Mansfield, P. 2015, *The Astrophysical Journal*, 813, 54, doi: [10.1088/0004-637X/813/1/54](https://doi.org/10.1088/0004-637X/813/1/54)

Trenti, M., Stiavelli, M., Bouwens, R. J., et al. 2010, *The Astrophysical Journal*, 714, L202, doi: [10.1088/2041-8205/714/2/L202](https://doi.org/10.1088/2041-8205/714/2/L202)

Vale, A., & Ostriker, J. P. 2004, *Monthly Notices of the Royal Astronomical Society*, 353, 189, doi: [10.1111/j.1365-2966.2004.08059.x](https://doi.org/10.1111/j.1365-2966.2004.08059.x)

van der Velden, E. 2020, *The Journal of Open Source Software*, 5, 2004, doi: [10.21105/joss.02004](https://doi.org/10.21105/joss.02004)

Viel, M., Haehnelt, M. G., & Springel, V. 2004, *Monthly Notices of the Royal Astronomical Society*, 354, 684, doi: [10.1111/j.1365-2966.2004.08224.x](https://doi.org/10.1111/j.1365-2966.2004.08224.x)

Virtanen, P., Gommers, R., Oliphant, T. E., et al. 2020, *Nature Methods*, 17, 261, doi: [10.1038/s41592-019-0686-2](https://doi.org/10.1038/s41592-019-0686-2)

Wang, F., Yang, J., Hennawi, J. F., et al. 2023, *The Astrophysical Journal Letters*, 951, L4, doi: [10.3847/2041-8213/accd6f](https://doi.org/10.3847/2041-8213/accd6f)

Weinberger, L. H., Haehnelt, M. G., & Kulkarni, G. 2019, *Monthly Notices of the Royal Astronomical Society*, 485, 1350, doi: [10.1093/mnras/stz481](https://doi.org/10.1093/mnras/stz481)

Wilkins, S. M., Lovell, C. C., Vijayan, A. P., et al. 2023, *Monthly Notices of the Royal Astronomical Society*, 522, 4014, doi: [10.1093/mnras/stad1126](https://doi.org/10.1093/mnras/stad1126)

Zhu, H., Gnedin, N. Y., & Avestruz, C. 2024, *The Astrophysical Journal*, 975, 115, doi: [10.3847/1538-4357/ad793c](https://doi.org/10.3847/1538-4357/ad793c)

Zhu, Y., Becker, G. D., Christenson, H. M., et al. 2023, *The Astrophysical Journal*, 955, 115, doi: [10.3847/1538-4357/accef4](https://doi.org/10.3847/1538-4357/accef4)

Zhu, Y., Becker, G. D., D'Aloisio, A., et al. 2026, *The Astrophysical Journal*, 1002, 93, doi: [10.3847/1538-4357/ae5bbb](https://doi.org/10.3847/1538-4357/ae5bbb)

APPENDIX

A. IMPACT OF DUTY CYCLE TIMESCALE

In this appendix we detail the impact that changing the duty cycle, defined in Eq. (6), has on the projected autocorrelation function χ_V and the galaxy–Ly α transmission cross-correlation δ_F . We explore three additional duty cycles, $\Delta t = 25, 100$ and 200 Myr.

In Fig. 8, we show the projected autocorrelation χ_V at $z = 6$. Modulo scatter at small r_\perp , which is largely due to small numbers of haloes at these separations, the effect of increasing the duty cycle is to increase χ_V across all r_\perp . This is easily understood because, at fixed galaxy luminosity, increasing (decreasing) the duty cycle tends to increase (decrease) the mass of halo hosting that galaxy. Larger mass haloes tend to cluster more strongly, hence the behaviour of χ_V as a function of Δt . The behaviour is similar for the entire range of redshifts that we consider in this work.

In Fig. 9 we show the galaxy–Ly α transmission correlation δ_F for these additional duty cycle timescales. We have used a bin size four times smaller than that used in Fig. 5 to highlight the differences between the different duty cycle timescales at small r . The differences between the different duty cycle timescales are very small, and manifest mostly at $r \lesssim 10$ cMpc, where a longer duty cycle timescale tends to decrease δ_F . As described earlier in this appendix, and demonstrated in Fig. 10, where we show the distribution of halo masses used in the calculation of δ_F for each duty cycle timescale Δt , increasing the duty cycle tends to increase the typical halo mass for a given galaxy luminosity. As shown in Conaboy et al. (2025), this leads to a decrease in δ_F at

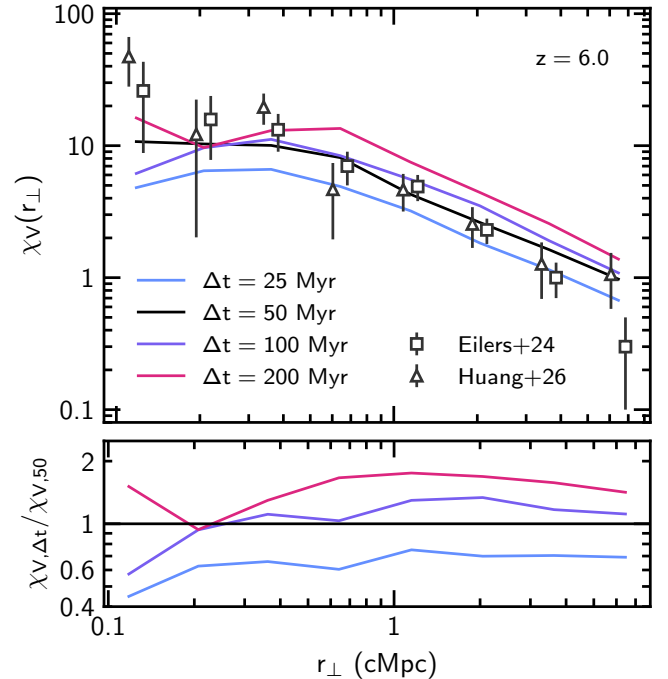


FIG. 8.— Projected autocorrelation function χ_V of [O III] emitters at $z = 6$ (top panel) for our fiducial duty cycle $\Delta t = 50$ Myr (black), as well as for duty cycles of $\Delta t = 25, 100$ and 200 Myr (blue, purple and pink, respectively), along with observational constraints due to Eilers et al. (2024) (grey squares) and Huang et al. (2026) (grey triangles). We also show the ratio of χ_V for each of these duty cycles to χ_V for our fiducial choice of $\Delta t = 50$ Myr (bottom panel).

$r \lesssim 10$ cMpc. Conaboy et al. (2025) also showed that the behaviour at larger r is complicated by the competing

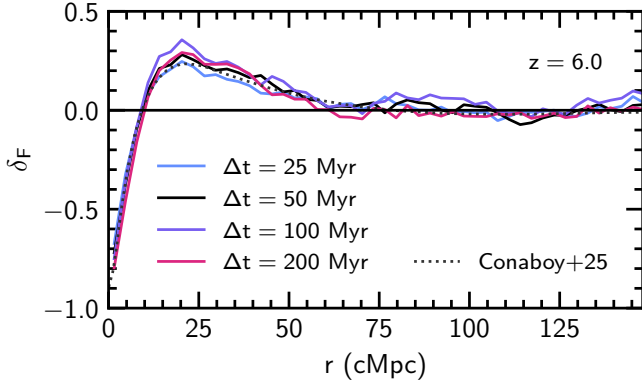


FIG. 9.— Galaxy–Ly α transmission correlation at $z = 6$ for our fiducial duty cycle $\Delta t = 50$ Myr (black), as well as for duty cycles of $\Delta t = 25, 100$ and 200 Myr (blue, purple and pink, respectively), along with the distribution from Conaboy et al. (2025) (grey dotted).

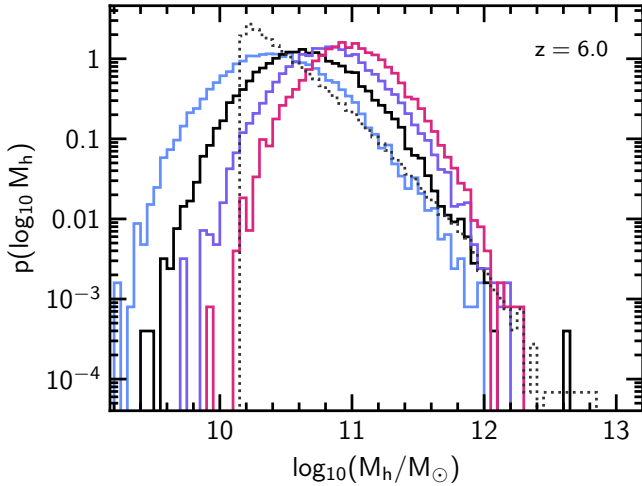


FIG. 10.— Distribution of halo masses used to compute δ_F at $z = 6$ for our fiducial duty cycle $\Delta t = 50$ Myr (black), as well as for duty cycles of $\Delta t = 25, 100$ and 200 Myr (blue, purple and pink, respectively), along with the distribution from Conaboy et al. (2025) (grey dotted). The line styles are as in Fig. 9.

effects of density and photoionisation rate enhancement around more massive galaxies, and in this work we find that the scatter between different timescales means that we observe no clear dependence on Δt for $r \gtrsim 10$ cMpc. Fig. 4 shows that the typical halo mass used to compute δ_F differs by about ~ 0.8 dex between the shortest and longest timescales, and that the distribution of masses covers similar ranges. This explains why the difference in δ_F for the different timescales is small.

B. IMPACT OF HALO FINDER ON SMALL-SCALE CLUSTERING

In this appendix we discuss the impact of our choice of halo finder on the small-scale clustering of galaxies. In Fig. 11 we show the volume-averaged projected auto-correlation function χ_V (see Sec. 2.2.3) at $z = 6.2$, using our fiducial abundance-matched FoF halo catalogue (taking the fiducial luminosity cut of $\log_{10}(L_{[\text{O III}]}) > 42.4$) and also for a reanalysis of the snapshot using ROCKSTAR (Behroozi et al. 2013). For the ROCKSTAR case, we include all (sub)haloes more massive than

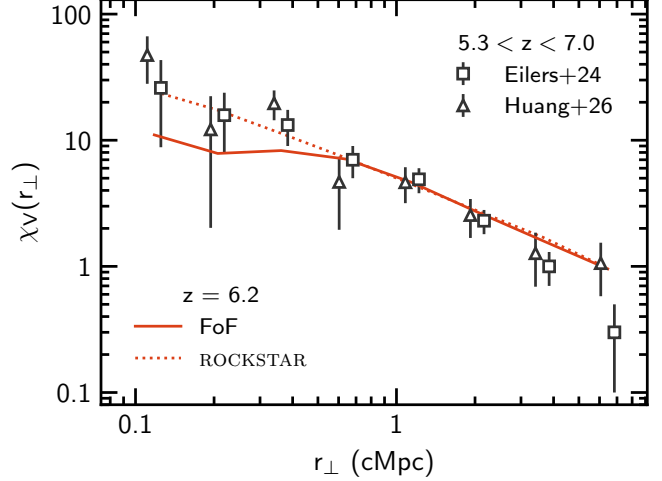


FIG. 11.— Comparison of χ_V at $z = 6.2$ estimated using our fiducial FoF halo catalogue (solid line) and using a ROCKSTAR catalogue (dotted line). Also shown are observational constraints due to Eilers et al. (2024) (grey squares) and Huang et al. (2026) (grey triangles).

$\log_{10}(M_h/h^{-1} M_\odot) > 10.5$, where this lower mass limit is chosen to reproduce our abundance-matched χ_V for $r_\perp > 1$ cMpc. We find that, for $r_\perp \lesssim 0.4$ cMpc, where the slope of χ_V for our fiducial catalogue flattens, the ROCKSTAR catalogue is in good agreement with observational constraints. As described in Sec. 2.2.3, ROCKSTAR – unlike FoF used with a single linking length – provides information about substructure and hence on galaxies that can occupy the same halo. We can therefore attribute the poorer agreement between our fiducial catalogue and the observational data at small projected distances to this missing contribution from galaxies inside the same halo. Note that we do not use the ROCKSTAR catalogue for our main analysis, since the underlying radiative transfer simulation used the FoF catalogue to determine the location of ionising sources, and so changing catalogues would break the spatial correspondence between halo and source location.

This paper was built using the Open Journal of Astrophysics L^AT_EX template. The OJA is a journal which provides fast and easy peer review for new papers in the astro-ph section of the arXiv, making the reviewing process simpler for authors and referees alike. Learn more at <http://astro.theoj.org>.